Non-iterative Blind Deblurring of Digital Microscope Images with Spatially Varying Blur

Furkan Kaynar[1]([✉]) [iD], Peter Geißler[2] [iD], Laurent Demaret[3] [iD],
Tamara Seybold[4], and Walter Stechele[5] [iD]

[1] Chair of Media Technology, Munich Institute of Robotics and Machine Intelligence,
TU München, Arcisstr. 21 and Georg-Brauchle-Ring 60, Munich, Germany
furkan.kaynar@tum.de

[2] Munich Surgical Imaging, Türkenstr. 89, Munich, Germany
pgeissler@munichimaging.de

[3] Hochschule München, Dachauer Straße 98b, Munich, Germany
laurent.demaret@hm.edu

[4] ARRI Cine Technik, Herbert-Bayer-Str. 10, Munich, Germany
tseybold@arri.de

[5] Chair of Integrated Systems, TU München, Theresienstr. 90, Munich, Germany
http://www.ce.cit.tum.de/en/lmt/home/
http://www.munichimaging.de
http://www.me.hm.edu
http://www.arri.de
http://www.ce.cit.tum.de/en/lis/home

Abstract. One of the main limiting factors of image quality in surgical microscopy is of physical nature: resolution is limited by diffraction effects. The digitalisation of surgical microscopy allows computational solutions to partially compensate for this limitation of the involved optics. An inherent characteristic of microscope optics is that it is diffraction-limited which leads to blurred images of objects that do not lie in the (often very narrow) focus plane. Digital deblurring techniques can correct this during the surgical operation, however the point spread function is not constant spatially, making the problem complicated and extremely ill-posed. Most blind deblurring algorithms formulate an iterative solution to estimate the latent sharp image, which is not appropriate for processing high-resolution, high frame rate videos in real-time conditions. We propose a novel single-pass non-iterative blind deblurring method which estimates the spatially varying point spread function by evaluating structural details locally and performing deblurring only at pixels with significant structural information, avoiding noise amplification and decreasing computational cost. The quantitative and qualitative experiments showed the effectiveness and robustness of our method, indi-

cating the promising nature of image enhancement for microscopy-based surgical operations.

Keywords: Blind deblurring · Image restoration · Digital surgical microscopy · Medical image enhancement

1   Introduction

One of the main challenges of digital microscopy is to obtain images which have simultaneously low noise and a high resolution. For a diffraction limited surgical microscope system like the ARRISCOPE developed at Munich Surgical Imaging and Arnold and Richter Cine Technik, the effective width of the PSF is typically larger than the pixel sensor. This results in a loss of fine details and microscope images which aren't as sharp as desired, even if they lie in the focal image plane.

The shallow depth of field causes objects to appear unsharp on the image as soon as they slightly deviate from the focal image plane. The dependency of the blurring kernel on the 3D distance between the objects and the lens makes the modelling of the local PSFs and the design of appropriate deblurring methods complex.

The main advantage of digital microscopes is to enable real-time processing to adaptively deblur the image. The design of the new deblurring method introduced in this work is driven by these properties:

Adaptiveness: The solution should be adaptive and valid for images with varying sharpness, contrast and brightness.
Spatially Selective Deblurring: The deblurring algorithm should focus on areas close to the focus plane as the surgeon is mainly interested in these regions.
Real-time compatibility: The algorithms should be as parallelizable as possible, hence allowing real-time application.

2   Related Work

Non-blind deconvolution often relies on a preliminary calibration procedure to obtain an accurate model of the shift-invariant PSF. The PSF can be estimated using images of point-like targets with system specific diffraction models [14], [9], or by adapting traditional knife-edge (or slanted edge) techniques to digital devices as done by Reichenbach et al. [11]. In the absence of precise knowledge of the PSF, a joint estimation of the unknown image and of the blurring kernel is required. This results in a severely ill-posed inverse problem called blind deconvolution, which often admits multiple solutions. In surgical microscopy, the relevant anatomy is often not situated on a single plane: the narrow depth of field common to most microscopes, thus generates a strong defocus for the parts of the scene situated away from the focal object plane, resulting in an optical blur which depends on the distance between object and microscope, hence changing spatially in the scene. Furthermore this spatial variation depends on the object

and is therefore not constant over time in general, which makes it impossible to perform a pre-calibration. This leads to a new problem, the estimation of a spatially varying PSF which is extremely ill-posed. This problem has received some attention recently, often addressed in a more generic framework, not necessarily restricted to the microscopy application.

Over the last few decades, much research has been conducted on the minimisation of functionals with an image term and a PSF term for blind image deblurring. This leads to iterative methods which alternate *image restoration* steps with estimates of the blurring kernel, as in [3], where the classical Richardson-Lucy iteration [12] is applied to the problem of blind deconvolution. Sun et al. [17] use an image patch-based iterative optimization technique to estimate the spatially invariant PSF. Joshi et al. [5] estimate a spatially varying PSF from a single image. To this end, a cost function with a fidelity term and a penalty term for the smoothness of the PSF is minimized. After the PSF is estimated, the sharp image is recovered by using the Richardson-Lucy deconvolution algorithm. Michaeli et al. [7] propose an iterative minimisation where a patch-based image prior is added to a traditional data fidelity/smoothness functional.

In order to deal with the problem of spatially varying PSF, some authors used more classical edge extraction techniques, implicitly exploiting the valuable information contained in the local sharpness of edges. In [8] and [18], the original (unknown) edges are assumed to be ideal step edges. The spatially varying blur is modelled by a (spatially varying) Gaussian kernel: the estimate of the local PSF amounts to estimating the variance of the kernel which is done by using an unsharp masking approach. Smith [16] examines parametric models to fit on edge profiles through the gradient descent approach. Edge model fitting is preferred for estimating the PSF, because it reduces the noise amplification due to the differentiation step. A non-parametric and spatially invariant blur kernel is estimated using edge profiles in [2], leading to a Radon transform-based PSF estimation.

3   Image Blurring Model

Image blurring is usually modeled as the convolution of the ideal image with the point spread function (PSF), which describes how a point light source spreads on the image plane [15]. The degraded image additionally contains additive noise. The narrow depth of field typical of microscopy results in a PSF varying in space, which leads to the following image blurring model:

$$g(x,y) = \iint\limits_{m,n} I(x-m, y-n)\, p(m,n,x,y)\; dm\; dn + \; \eta(x,y) \qquad (1)$$

where g is the observed degraded image, I is the (unknown) ideal image, p is the PSF, η is the additive noise, and m, n denote the pixel indices. Due to the extreme ill-posedness of this problem, we will need to introduce some simplifying assumptions in order to obtain a solution:
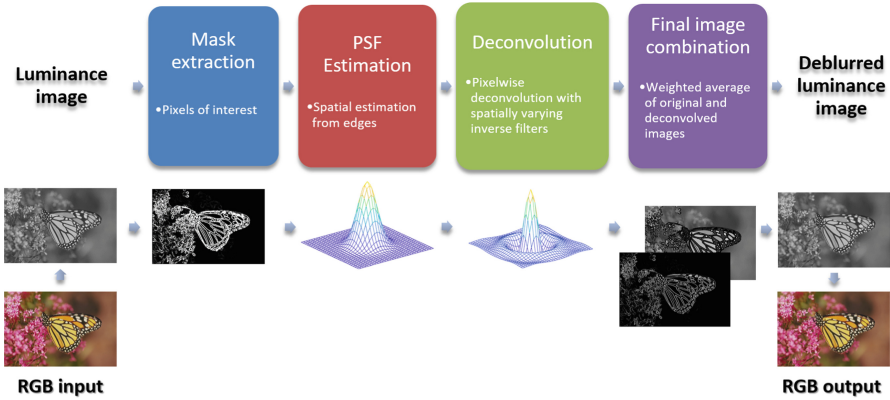
Fig. 1. Overview of the proposed deblurring scheme. The algorithmic steps are detailed in Sects. 4.1 to 4.4

Step Edge Assumption. It is assumed that the observed edges stem from ideal sharp edges, mathematically modelled as discontinuities along lines. In spite of some limitations in the biological context (e.g. intrinsically "unsharp" tissues), the approximation made by this model turns out to be accurate enough for practical purpose.

PSF Isotropy. Since we do not deal with motion blur, we assume that the PSF of the system can be approximated by an isotropic model. The optical PSF of lenses tend to be anisotropic at the image borders [6], however we assume that the regions of interest lie in the central areas of the image.

Use of Luminance Image. After applying a luminance/chrominance decomposition, the structural details are mostly concentrated in the luminance component. It is therefore straightforward to deblur exclusively the luminance channel, which also reduces chromatic aberration and color artefacts. Since the luminance image is a weighted average of the three color channels, the noise variance in the luminance image is smaller than the noise variances of each single individual color channel, which helps to avoid noise amplification as well.

4   Proposed Method

In order to recover the original image I from data g we need the blurring kernel at each pixel. The local condition of the problem is particularly bad in smooth areas, with no or few anatomical structure. Since in these areas deblurring is not necessary and leads to noise amplification, our method is designed such as performing no deblurring in the flat, information-sparse areas. Our local adaptive deblurring method is summarized in Fig. 1 and consists of the following steps:

A. Determination of the pixels of interest. The set of pixels on which the deblurring will be performed are extracted according to the (estimated) amount of information close to each pixel.

B. Local PSF estimates. The spatially varying PSF is estimated from the edges of the luminance image using an appropriate blur kernel model.

C. Deconvolution on the region of interest. The actual deconvolution applies the PSF estimates (step B) on the area selected at step A.

D. Formation of a global deblurred image. The deconvolved image is combined with the original image by using suitable weighting. This results in a coherent reconstruction of the image on the whole image domain.

4.1 Determination of the Pixels of Interest

The deconvolution of flat image areas leads to an amplification of noise without providing additional valuable information. In order to deblur only areas with structural information, we create a mask M which associates a value $M(p)$ between 0 and 1 with each pixel. The final recovered image is then obtained by combining the (locally) deconvolved image and the original image:

$$I_{final} = M \odot I_{deconvolved} + (1 - M) \odot I_{input} \qquad (2)$$

where $\odot$ is the element-wise multiplication.

In practice, images are noisy, which makes a naive use of gradients difficult: a preliminary edge-preserving denoising step is therefore necessary. The mask extraction should also be adaptive to the image contrast level which can differ from one input image to another. Hence, we apply an adaptive contrast stretching step to obtain the final mask. The proposed mask extraction algorithm consists of the following three steps:

– **Edge-preserving denoising** of the luminance channel by a modified non-iterative version of the anisotropic diffusion of Perona and Malik [10].
– **Structure map extraction**. The information on edges and textures is extracted by using the structure tensor of the image.
– **Adaptive contrast stretching** is applied to the structure map in order to take into account the contrast heteoregeneity over the image.

Edge-preserving Denoising. The preliminary denoising step needs to preserve the edges. To this end, we use the first iteration of a modified version of Perona-Malik non-linear diffusion method [10]. The Perona-Malik filtering relies on the use of a non-constant diffusivity, small at edge locations. The local amount of edge information is measured by the norm of the gradient $\|\nabla I\|$ and leads to a diffusion equation of the form:

$$\frac{\partial I}{\partial t} = \mathtt{div}\left(c\left(\|\nabla I\|^2\right)\nabla I\right) \qquad (3)$$

where $c : \mathbb{R}^+ \to \mathbb{R}^+$ is a positive decreasing function, for instance

$$c(s^2) = e^{-\frac{s^2}{\kappa}} \tag{4}$$

In this work we apply only the first iteration of a numerical procedure to solve the diffusion equation. Furthermore we modify the used diffusivity in order to take into account the local directionality in the image.

Structure Map Extraction. In order to generate a mask with high values in presence of structures and low values in the smooth image areas, we first compute the structure tensor [4] to analyse the local image anisotropy. The structure tensor $S_w(i,j)$ at a pixel (i,j) is defined as follows:

$$S_w(i,j) = \begin{bmatrix} \sum_w I_x^2 & \sum_w I_x I_y \\ \sum_w I_x I_y & \sum_w I_y^2 \end{bmatrix} \tag{5}$$

where $\sum_w$ indicates the weighted averaging of the values in the local neighborhood w, I_x and I_y are discrete approximations of the partial derivatives. The weighted averaging is done by applying a 2D Gaussian filter. The eigenvalues of the positive semidefinite symmetric matrix S_w describe the average contrast in the directions of its eigenvectors. The difference between the eigenvalues is a valuable quantitative indicator on how much structure is contained at this pixel [19]. We define the structure map $C(i,j)$ as follows:

$$C(i,j) = \lambda_1 - \lambda_2 \tag{6}$$

where $\lambda_1 \geq \lambda_2$ are the eigenvalues of the matrix $S_w(i,j)$. We do not normalize this coherence metric in order not to lose the global contrast information and not to amplify the noise in the flat image regions.

Adaptive Contrast Stretching. Once the structure map is obtained, we apply adaptive global contrast stretching in order to deal with different input image contrasts. To this end, we use unimodal thresholding (Rosin's method [13]) based on the histogram of the structure map. The obtained threshold T is used to decide whether a contrast level is significant or not. The final mask C_N is obtained by applying the following smooth thresholding strategy to the structure map C:

$$C_N(i,j) = \begin{cases} 1.0 & C(i,j) \geq T \\ C(i,j)/T & C(i,j) < T \end{cases} \tag{7}$$

It ranges in $[0,1]$ and allows for a smooth combination of the input and deconvolved images at the last step of our deblurring method. Our experiments show that the mask extraction is quite robust and stable under a wide range of contrast levels, as desired. We also tested the performance of mask extraction under simulated Gaussian noise and observed that the extraction remains robust also at noise levels higher than those measured in real images.

4.2   Spatially-Varying PSF Estimation

The actual PSF of a surgical microscope depends on the distance of the objects to the focus plane of the imaging system, which makes it impossible to perform a global 3D-calibration of the PSF. In this work, the PSF (varying spatially and in time) is estimated locally, in real time. Our model for the PSF relies on an isotropic and unimodal 2D function. We estimate the PSF at the locations where a blurred edge has been previously detected, based on the 1D profile perpendicular to the edge, which is also called the edge spread function (ESF).

Analytical PSF Modeling and Estimation. The line spread function (LSF), obtained by differentiating the ESF is the one dimensional equivalent of the PSF [20]. The reconstruction from the observed ESFs is ill-posed. We are facing the following issues:

– Direct reconstruction yields a noisy PSF due to the noise amplification by the differentiation of the ESF.
– The resolution of the reconstructed PSF is limited by the digital sensor resolution.

These observations led us to fit an edge model to the edge profile and reconstruct the PSF analytically as in [16], rather than directly reconstructing it via the observed ESFs. Since the ESF and the PSF have an analytical relation, we start with selecting the PSF model depending on the optical PSF of a diffraction-limited imaging system.

In order to model the PSF, we use a simple isotropic bivariate Gaussian function centered at the origin.

$$p(x, y) = \frac{1}{2\pi\sigma^2} e^{-\frac{x^2+y^2}{2\sigma^2}} \tag{8}$$

where x and y indicate the horizontal and vertical coordinates.

The PSF estimation problem thus amounts to estimating the spatially varying σ values along the image. The σ values are only estimated at pixels located on the edges at some pixels of the image and the initially estimated PSF map is called "sparse σ-map". After an outlier correction step, the sparse σ values are interpolated to obtain a continuous blur map. If the PSF model is an isotropic bivariate Gaussian function with a given σ, then the LSF of any orientation is a univariate Gaussian function with the same σ, and the ESF model to fit to the edge profiles is given as the cumulative distribution function of the normal distribution, given by

$$e(x) = \frac{1}{2}\left[1 + erf\left(\frac{x - x_0}{\sigma\sqrt{2}}\right)\right] \tag{9}$$

where erf is the error function.

Steps to Estimate the Sparse σ-map:
Let us summarize the main steps to estimate the sparse σ-map.

– Image edges are detected using an edge detector like Canny detector [1].
– For each pixel location on the edge map, the ESF values are calculated from the luminance image through bilinear interpolation for the locations on the perpendicular line to the edge.
– The extracted edge profile may include structural details not belonging to the edge. For robust model fitting, we isolate the central part of the edge profile as in [8].
– We use a threshold based on the total variation (TV) of the isolated edge: edge profiles below the threshold are dropped without estimating the σ at this image location.
– For model fitting, we compute the subpixel location m, corresponding to the middle point of the ESF model to be fitted. The local value of σ is then estimated by least square minimisation.

4.3   Deconvolution Filter Design

After estimating the spatially varying blur, we perform a non-blind deblurring step, by using non-linear locally adaptive filters based on the classical $2D$-Wiener deconvolution filter, together with a regularization factor. The proposed deconvolution filter is formulated in the frequency domain u, v as follows:

$$W(u,v) = \frac{1}{P(u,v)} \left[\frac{|P(u,v)|^2}{|P(u,v)|^2 + \frac{1}{SNR(u,v)^2}} \right] \tag{10}$$

where $P(u,v)$ is the Fourier transform of the PSF model $p(x,y)$ given in Eq. 8 with the locally estimated σ value. We need to take in to account that the SNR value varies spatially along the image, because the image sensor has a signal dependent noise. Hence, we use a regularized model for the SNR, given as:

$$SNR(u,v)_{I_m,\alpha} = \frac{I_m^2}{(u^2 + v^2)^{\alpha/2} \, \sigma_Y^2(I_m)} \tag{11}$$

where I_m indicates the local intensity value and $\sigma_Y^2(I_m)$ is the intensity dependent noise variance, obtained by camera specific modelling, and α is a regularization parameter.

4.4   Deconvolution and Final Image Composition

In this step, the regions of the luminance image where the mask has values larger than a small threshold are deconvolved pixelwise with the locally corresponding spatial domain filter. As explained in the previous section, the deconvolution filter depends on the intensity value of the center pixel, the estimated σ value at that pixel, the simulated noise power $\sigma_Y^2(i)$ and the selected α parameter. Finally, the deconvolved image is averaged with the input image using the mask weights as shown in Eq. 2.

5   Experiment Results

Quantitative and qualitative experiment results are discussed in this section. Quantitative analysis of estimation accuracy of the sparse σ-map for different inter-edge distances, orientations and noise levels are given. Only qualitative analysis can be performed on real word microscope images, since the sharp ground truth images are inherently non-accessible.

5.1   Quantitative Analysis of Blur Map Estimation

Ideal gray-scale patterns are blurred with isotropic bi-variate Gaussian kernels according to synthetic ground truth σ-maps. Based on the blurred images, we estimate the sparse σ-map and analyze the accuracy of the estimation under different conditions. Note that we analyze the accuracy of the sparse σ-map on the pixel locations where the PSF estimation was performed, and we do not analyze the interpolated σ-map since the edge-aware interpolation step depends on the image content. Test images with constant (bar type) or varying edge orientation (circle type) are used.

Influence of Inter-edge Distance. To test the accuracy of σ estimation under varying inter-edge distances, bar patterns with different bar widths are created and blurred using the ground truth σ-map given in Fig. 2d The ground truth σ values vary from 0.5 to 2.5.

(a) Bar width 5px   (b) width 10px   (c) width 20px   (d) Ground truth
σ-map

(e) Estimated and   (f) Estimated and ground   (g) Estimated and
ground truth σ (5px)   truth σ (10px)   ground truth σ (20px)
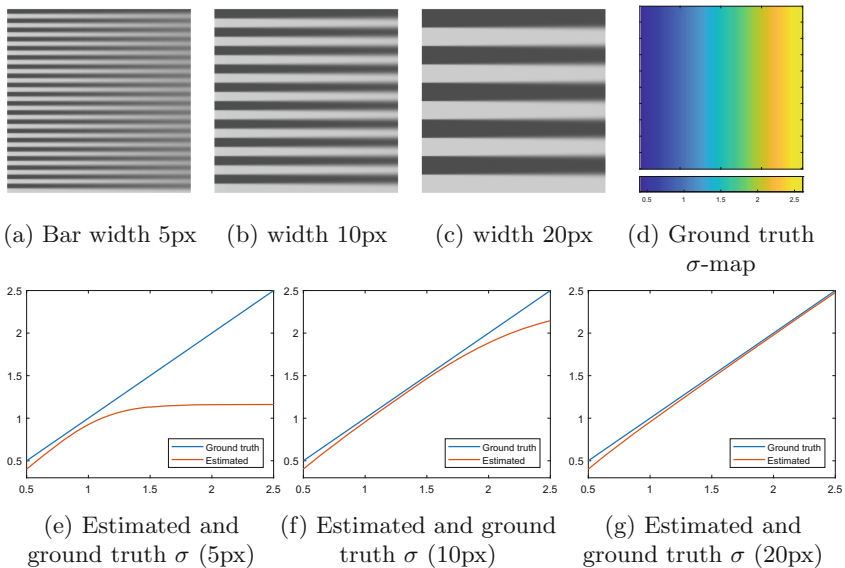
Fig. 2. Influence of inter-edge distances on the σ estimation (Color figure online)

Blurry results are given in Figs. 2a,b,c and the corresponding estimation results are plotted underneath with red color, while the ground truth values are shown with blue color. We observe that there is an upper limit of correctly estimated blur kernel width, and this limit is determined by the inter-edge distances.
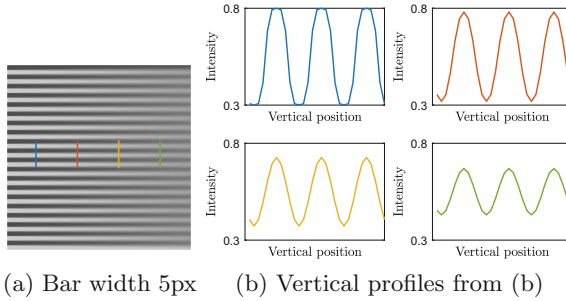

(a) Bar width 5px   (b) Vertical profiles from (b)

Fig. 3. Blurred bars with different widths and their profiles

If the PSF is wider than the inter-edge distance, the spread of an edge pixel affects the intensity values of neighboring edges and the edge contrasts decrease. In this case, PSF estimation yields smaller σ values due to edge contrast normalization in the next step. This effect is shown in Fig. 3 with the edge profiles extracted from the blurry image at different blur levels. Fortunately, this limitation does not lead to visible artifacts, on the contrary it yields better visual results than deblurring the close edges with large kernels.

Influence of Edge-Orientations. The blur estimation accuracy at different edge orientations is tested with a circle pattern, blurred with different kernels according to the σ-map in Fig. 4a. Edge map and sparse σ-map are estimated at edge locations. Estimation results at different orientation angles are shown in Fig. 4c with red color.
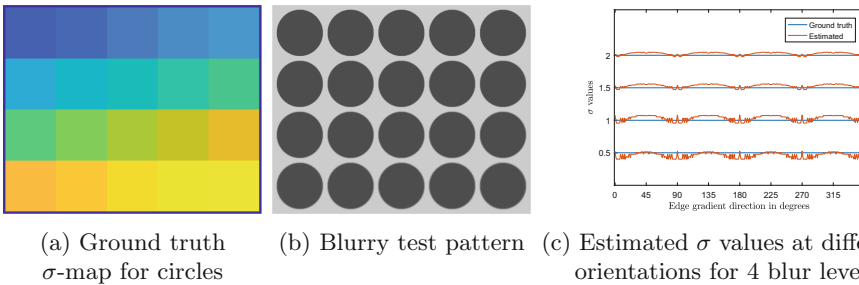

(a) Ground truth   (b) Blurry test pattern (c) Estimated σ values at different
σ-map for circles   orientations for 4 blur levels

Fig. 4. Blur map, test pattern, and σ estimation for different edge orientations (Color figure online)

We observe that the estimation accuracy varies at different angles, due to the discrete grid nature of image pixels. We also observe that the estimation accuracy increases with increasing blur kernel size. This is reasonable because smaller kernels are discretized with fewer samples, leading to more severe discretization effects. We observe that the estimation errors remain at acceptable levels: The absolute deviation from the ground truth values is mostly smaller than 0.1.

Influence of the Additive Noise. In this section, the estimation accuracy will be tested using the blurred bar patterns contaminated with zero-mean additive white Gaussian noise.
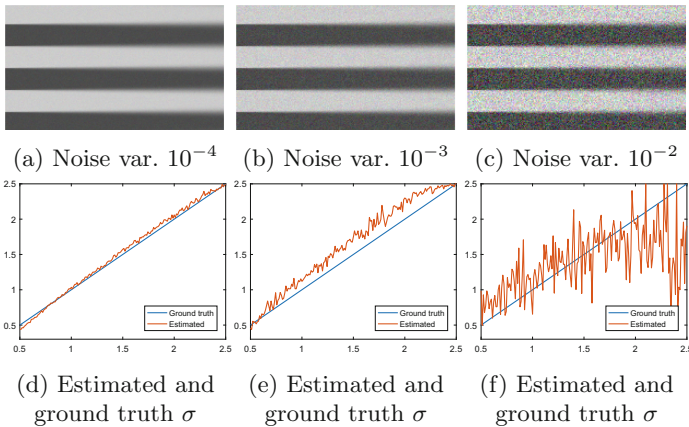

(a) Noise var. 10^{-4} (b) Noise var. 10^{-3} (c) Noise var. 10^{-2}

(d) Estimated and ground truth σ (e) Estimated and ground truth σ (f) Estimated and ground truth σ

Fig. 5. σ estimation with additive white Gaussian noise

In Fig. 5, we observe that the accuracy of σ estimation is acceptable for low-level and mid-level noise, and it decreases significantly for strong noise. Strong noise may cause false positive edge detections in flat areas, and it could affect the σ-estimation. These results indicate that the deblurring algorithm must be designed differently for the strong noise. However, deblurring strongly noisy images is out of our interest since the images obtained by the ARRISCOPE have much weaker noise than the high-level noise we used in the experiments.

5.2 Qualitative Analysis of Deblurring

In this section the experiment results for the real microscope images taken by the ARRISCOPE are given. We discuss results for a test image and a surgical image.

– **Test chart image:** This image shows the fine details printed on a flat test chart (Fig. 6). We can qualitatively estimate the original signal and assess the deblurring performance due to the basic structures in the image.

– **Surgery image:** This image was taken during a microsurgical operation and reflects the nature of images including biological tissues (Fig. 6).
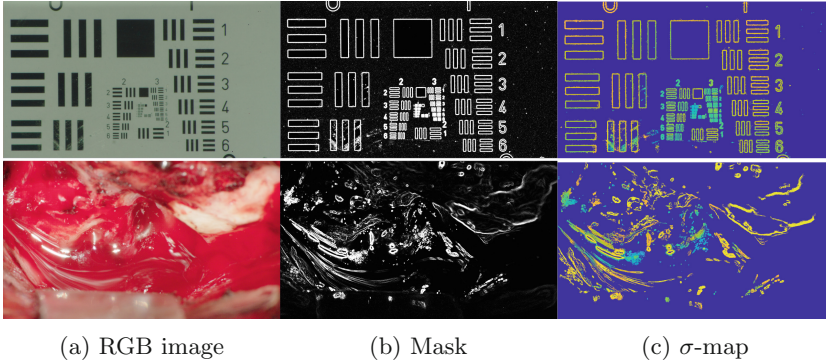
5.3 Mask and σ-map Results

(a) RGB image   (b) Mask   (c) σ-map

Fig. 6. Test chart and surgery image, mask and σ-map. σ ranges from 0 (blue) to 2.5 (yellow). (Color figure online)

In Fig. 6 we observe that the extracted masks successfully select the regions to deblur. The sparse σ values are interpolated in the regions where the mask values ($\in [0, 1]$) are larger than a small threshold (0.2 in our application). The obtained masked interpolation results are given alongside the masks. Note that smaller σ values are estimated on finer details, but results in less visual artefact as explained in Sect. 5.1.

In addition to the imaging parameters of the camera, we have many parameters for individual steps in the deblurring algorithm. As the performance of algorithm depends on the input image content, we cannot determine optimal parameter values valid for all possible images, but we can examine the effects of several critical parameters which cause remarkable difference in the final deblurring results. For this aim, we will examine the effects of selecting the frequency gain regularization parameter α of the Wiener deconvolution and the influence of increasing upper limit of the σ-map.

5.4 Influence of the Selection of α

As expressed in Sect. 4.3, the frequency attenuation parameter α is used to obtain the frequency dependent SNR functions and to have a better regularization of high frequency noise. This parameter changes the overall perceived sharpness level and it can be used as the single parameter to tune the deblurring strength during a surgical operation. For the analysis of α values, the upper limit of σ is set as 1.7, which is an intermediate value for the resolution of our test images. The

effects of different upper limits for the σ-map will be analyzed in the subsequent section, for a selected α value.

In the Fig. 7 the experiment results are given using varying α values. As expected, small α values yield sharper images but with more visual artifacts. The experiments show that an α value of 0.8 yields good results for both test images.
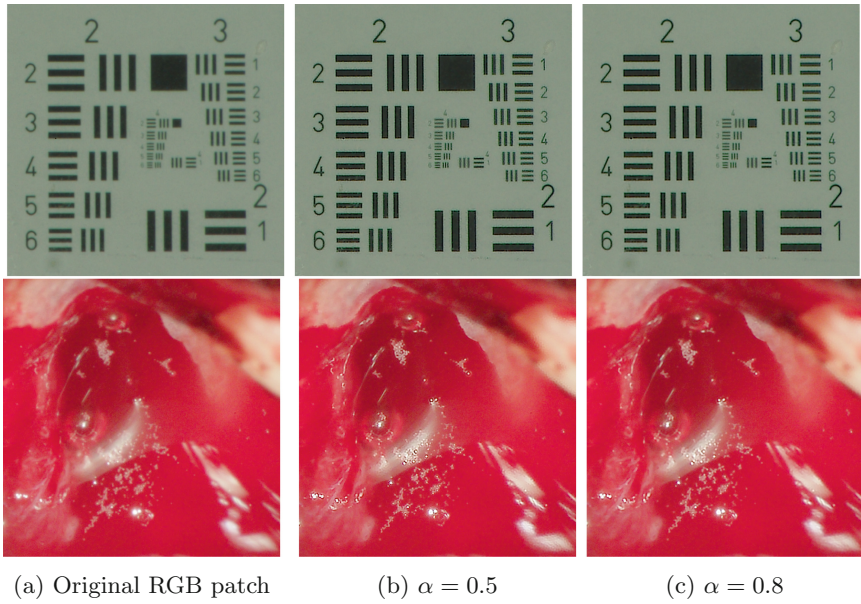

(a) Original RGB patch   (b) $\alpha = 0.5$ (c) $\alpha = 0.8$

Fig. 7. Test chart and surgery image patches with varying α values

5.5 Influence of the Upper Limit for σ-map

The estimated sparse σ-map values are clipped after outlier correction for several reasons. Too large σ values tend to be erroneous estimations and create visible artifacts in the image. Since our aim is not deblurring strongly blurred patterns, but to increase the visibility of fine details, very large σ values can be skipped. Clipping high σ values improves the robustness of the PSF estimation in shading areas. Based on experiments we chose a dual threshold method: all σ values above this shading threshold are eliminated, whereas σ values between the upper limit and the shading threshold are set to the upper limit. Results are given in Fig. 8. The shading threshold is constantly set at 3.5. The choice of the upper σ limit changes the deblurring results significantly, as different deconvolution filters are selected pixelwise. To reveal the effect of the upper limit, we first give the interpolated mask results for the surgery image with varying upper limits.

In the Fig. 8a, almost an uniform PSF is obtained, because the upper limit is very small and it clips most of the σ values in the map. As the upper limit

increases in the further figures, clipping is observed on blurry edges which have higher σ values. The change in the deblurring results is exemplified with the patches in Fig. 9. For deblurring, alpha is set to 0.8.
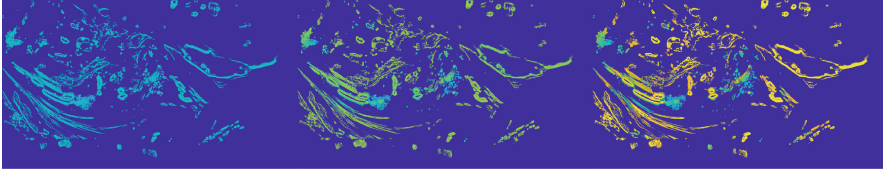
(a) Upper σ limit = 1.2   (b) Upper σ limit = 1.7   (c) Upper σ limit = 2.5

Fig. 8. Estimated σ-maps with different upper limits

In the patches in Fig. 9, we observe that the deblurring of fine details does not change substantially with varying upper σ limit, while the more blurry areas in the southeast region are affected, as they are deconvolved using larger kernels with increasing upper limit. This is due to the fact that the original σ values on these blurry regions are higher than the clipping limit in every patch given in the figure.
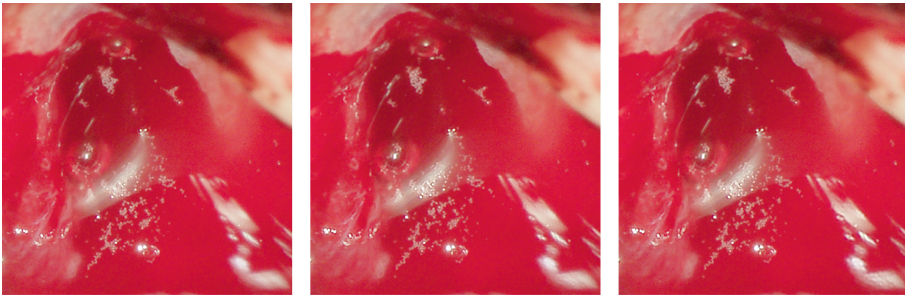
(a) Upper σ limit = 1.2   (b) Upper σ limit = 1.7   (c) Upper σ limit = 2.5

Fig. 9. Deblurred patches using σ-maps with different upper limits

6   Conclusion

In this work, we proposed a solution to improve the perceived resolution of a surgical microscope. It performs automatic selection of the regions of interest, spatially varying PSF estimation and regularized deconvolution in a non-iterative and adaptive way. The key (and most expensive) steps of the algorithm, the sparse σ-map estimation and the pixelwise deconvolution, both rely on local operations which make parallelization possible for a real-time implementation.

Quantitative and qualitative experiments indicate that the proposed algorithm can work in a stable way on a variety of images with different characteristics and increase the visual details without amplifying the image noise. The algorithm can be further optimized for a real-time blind deblurring application in order to increase the perceived visual information during the surgical operations. Its design allows easy porting to massively parallel computing devices such as GPUs.

References

1. Canny, J.: A computational approach to edge detection. IEEE Trans. Pattern Anal. Mach. Intell. **6**, 679–698 (1986)
2. Cho, T.S., Paris, S., Horn, B.K., Freeman, W.T.: Blur kernel estimation using the Radon transform. In: CVPR 2011, pp. 241–248. IEEE (2011)
3. Fish, D., Brinicombe, A., Pike, E., Walker, J.: Blind deconvolution by means of the Richardson-Lucy algorithm. JOSA A **12**(1), 58–65 (1995)
4. Jaehne, B.: Digital Image Processing. Springer, Heidelberg (2005). https://doi.org/10.1007/3-540-27563-0
5. Joshi, N., Szeliski, R., Kriegman, D.J.: PSF estimation using sharp edge prediction. In: 2008 IEEE Conference on Computer Vision and Pattern Recognition, pp. 1–8. IEEE (2008)
6. Kee, E., Paris, S., Chen, S., Wang, J.: Modeling and removing spatially-varying optical blur. In: 2011 IEEE International Conference on Computational Photography (ICCP), pp. 1–8. IEEE (2011)
7. Michaeli, T., Irani, M.: Blind deblurring using internal patch recurrence. In: Fleet, D., Pajdla, T., Schiele, B., Tuytelaars, T. (eds.) ECCV 2014. LNCS, vol. 8691, pp. 783–798. Springer, Cham (2014). https://doi.org/10.1007/978-3-319-10578-9_51
8. Nasonov, A., Nasonova, A., Krylov, A.: Edge width estimation for defocus map from a single image. In: International Conference on Advanced Concepts for Intelligent Vision Systems. pp. 15–22. Springer (2015)
9. Nasse, M.J., Woehl, J.C.: Realistic modeling of the illumination point spread function in confocal scanning optical microscopy. JOSA A **27**(2), 295–302 (2010)
10. Perona, P., Malik, J.: Scale-space and edge detection using anisotropic diffusion. IEEE Trans. Pattern Anal. Mach. Intell. **12**(7), 629–639 (1990)
11. Reichenbach, S.E., Park, S.K., Narayanswamy, R.: Characterizing digital image acquisition devices. Opt. Eng. **30**(2), 170–177 (1991)
12. Richardson, W.H.: Bayesian-based iterative method of image restoration. JoSA **62**(1), 55–59 (1972)
13. Rosin, P.L.: Unimodal thresholding. Pattern Recogn. **34**(11), 2083–2096 (2001)
14. Sarder, P., Nehorai, A.: Deconvolution methods for 3-D fluorescence microscopy images. IEEE Sig. Process. Mag. **23**(3), 32–45 (2006)
15. Sibarita, J.B.: Deconvolution microscopy. In: Microscopy Techniques, pp. 201–243 (2005)
16. Smith, E.H.B.: PSF estimation by gradient descent fit to the ESF. In: Image Quality and System Performance III, vol. 6059, p. 60590E. International Society for Optics and Photonics (2006)
17. Sun, L., Cho, S., Wang, J., Hays, J.: Edge-based blur kernel estimation using patch priors. In: IEEE International Conference on Computational Photography (ICCP), pp. 1–8. IEEE (2013)

18. Tang, C., Hou, C., Song, Z.: Defocus map estimation from a single image via spectrum contrast. Opt. Lett. **38**(10), 1706–1708 (2013)
19. Weickert, J.: Anisotropic Diffusion in Image Processing, vol. 1. Teubner Stuttgart (1998)
20. Zhang, X., et al.: Measuring the modulation transfer function of image capture devices: what do the numbers really mean? In: Image Quality and System Performance IX, vol. 8293, p. 829307. International Society for Optics and Photonics (2012)